Tailoring Desolvation Kinetics Enables Stable Zinc Metal Anodes

Zhen Hou, Hong Tan, Yao Gao, Menghu Li, Ziheng Lu, and Biao Zhang**

Z. Hou, H. Tan, Dr. Y. Gao, Prof. B. Zhang
Department of Applied Physics, the Hong Kong Polytechnic University, Hung Hom, Kowloon, Hong Kong, P.R. China
E-mail: biao.ap.zhang@polyu.edu.hk

M. Li, Prof. Z. Lu
Shenzhen Institutes of Advanced Technology, Chinese Academy of Sciences, Shenzhen 518055, P.R. China
E-mail: zh.lu1@siat.ac.cn

Keywords: zinc metal anode, solvation sheath, desolvation energy, complexing agent, hybrid electrolyte

Low-cost and high-safety aqueous Zn ion batteries have been considered as promising alternatives to Li-ion batteries, provided that a stable Zn metal anode could be developed. The dendrite growth and the low Coulombic efficiency (CE) are the primary two issues afflicting the design of advanced Zn metal anode. Inspired by the complexing agent in the electroplating industry, acetonitrile (AN) is proposed as an electrolyte additive to guide the smooth growth of Zn. The enhanced intermolecular interactions between Zn^{2+} and the mixed H_2O/AN solvents lead to the supersaturating of adatoms on the current collector, as revealed by the complementary theoretical and experimental studies. Consequently, homogeneous nucleation and smooth growth of Zn are enabled for achieving exceptional stability up to 1000 cycles with an excellent CE of 99.64% on average. Application-wise, the incorporation of complexing agent in the electrolyte is fully compatible with the cathode while maintains the non-flammable nature for safe operation. The solvation chemistry regulation strategy provides a promising route to stabilize Zn metal anodes.

1. Introduction

Li-ion batteries (LIBs) have dominated the energy market of portable electronics due to their high energy density and long cycle life.[1,2] The large-scale application of LIBs is partly restricted by several issues, including the limited lithium reserves, high cost of raw materials

and safety issues originated from the flammable organic solvents.[3] Aqueous rechargeable batteries are regarded as promising alternatives for LIBs.[4] The utilization of water solvent in the electrolyte brings about significant advantages on the cost and safety. Moreover, superior power outputs could be achieved thanks to the fast ion transport in aqueous electrolyte.[5,6] Among them, zinc-ion batteries have received considerable interests as Zn metals possess a high volumetric capacity of 5851 mAh/cm^3, low redox potential (−0.76 V *vs*. SHE) and abundant reserves.[7-9] However, the low Coulombic efficiency (CE) and dendrites growth upon repeated Zn deposition/stripping process hinder its practical applications in rechargeable batteries.[10,11]

To overcome the above obstacles of Zn metal anodes, several strategies have been developed, including modifying electrode configurations[12-16], optimizing electrolyte formulations[17-21], and constructing protective layers.[22-25] These strategies have gained great success in preventing the preferential growth of Zn metal through guiding the deposition sites. Fundamentally, desolvation of Zn^{2+} sheath in the electrolyte occurs before the electrodeposition reaction takes place on the substrate. Thus, the Zn deposition behavior and morphology highly rely on the solvation structure of Zn^{2+}.[26] Nonetheless, the investigation into the effect of microstructure of Zn^{2+} in the electrolytes on Zn deposition/stripping process is rarely conducted. Highly concentrated aqueous electrolytes, such as 1 M $Zn(TFSI)_2$ + 20 M LiTFSI, are recently proposed as an effective approach to inhibit H_2 evolution from water, and meanwhile improve CE of deposition/stripping.[27,28] The alternation of solvation sheath from H_2O molecular to the anions ($TFSI^-$) leads to much improved electrochemical performances, although the adoption of concentrated electrolytes would inevitably increase the cost.

It is worth noting that tremendous efforts have been devoted to manipulating the solvation structure of metal ion to achieve smooth coating in conventional electroplating industry.[29-31] For instance, the electrodeposition coating of Zn obtained from a simple salt solution, where a hydration shell is formed around Zn^{2+}, commonly presents coarse grain size, loose and uneven

structure. The small desolvation energy required for such solvation structure renders low nucleation overpotential and scarce nucleation seeds.[32,33] Therefore, the complexing agents, such as cyanide (CN^-), are generally used to regulate the solvation structure of Zn^{2+}, in which Zn^{2+} is solvated by CN^- instead of water due to stronger solvation ability between Zn^{2+} and CN^-.[34-36] Accordingly, this solvation structure results in the high nucleation overpotential and increased electrochemical polarization, in turn increasing the number of nucleation sites and enabling smoother metal film.[37]

Inspired by this mechanism, it is expected that regulating the solvation sheath of Zn^{2+} using complexing agents should be a promising approach to guide Zn^{2+} deposition behavior in Zn ion batteries. However, shifting from electroplating technology to rechargeable batteries is not straightforward, as the latter requires repeated deposition/stripping while the former only focuses on the initial Zn growth on the substrate. Moreover, the candidate complexing agent should be compatible with the demand for the wide electrochemical window and non-flammability of an electrolyte. After careful screening, acetonitrile (AN, CH_3CN), which has a similar chemical structure with cyanide (CN^-), is identified as an appropriate electrolyte additive without bringing any detrimental effects. The strong solvation capability of AN increases the number of nucleation sites and realizes dendrite-free morphologies of Zn. As a result, a prolonged cycle life of ~650 h at 2 mA/cm^2 under 50% of the depth of discharge (DOD) (cycling capacity of 2 mAh/cm^2) is achieved in hybrid water/AN electrolyte (HWAE-15, the number denotes the volume percentage of AN in the solvent). Moreover, the cell shows a high average CE of ~99.64% for ~2000 h at 2 mA/cm^2 with a cycling capacity of 2 mAh/cm^2 in HWAE-10.

2. Results and Discussion

We first examine the interaction between water and AN. The FTIR spectra for the various ratios of hybrid water/AN mixtures (HWA-X) are presented in Figure S1. After mixing, the O-H

stretching vibration in H_2O undergoes a blue shift from ~3334 cm^{-1} to ~3362 cm^{-1}, indicating AN has an impact on the hydrogen bonds of water. Meanwhile, the peak of C≡N stretching vibration (2252 cm^{-1}) in pure AN shifts to higher wavenumbers (2260 cm^{-1}) in HWAs. According to previous works, these observations are attributed to the formation of hydrogen-bonded acetonitrile molecules (O–H···N) between water and AN.[38,39] To investigate the interaction between Zn^{2+} and AN, the FTIR of HWAE-X are collected. As shown in Figure S2, when $ZnSO_4$ is added, a new peak emerges at 2283 cm^{-1}, and the peak at 2260 cm^{-1} experiences a slight red shift, implying the generation of AN-Zn^{2+} solvation structure. It reveals the interaction of AN with H_2O and Zn^{2+}, thus altering the solvation structure of the electrolyte.

To further understand the effect of AN addition on microscopic structures of electrolyte, first-principles calculations are carried out. The structure of the first solvation sheath is firstly evaluated by calculating the dissociation energies (E_d) of the $Zn(H_2O)_x(AN)_{6-x}^{2+}$ complexes. Such values reflect the strength of the interactions between the Zn^{2+} cation and the molecules in its first solvation sheath and therefore are good indicators of the solvation ability of the corresponding electrolytes. As shown in **Figure 1**a, E_d of the $Zn(H_2O)_6^{2+}$ solvation complex is 17.2 eV or 1654 kJ/mol, in good agreement with the hydration energy of the Zn^{2+}.[40,41] Such an E_d is significantly smaller than those of the complexes containing ANs, indicating the AN molecules have a much stronger affinity to the Zn^{2+} and inclusion of ANs in the electrolyte may significantly change the solvation structure of Zn^{2+}. In fact, by further calculating the incremental dissociation energy of E_d, we found that exchanging the water molecules with ANs in $Zn(H_2O)_x(AN)_{6-x}^{2+}$ is always energetically favorable for all possible x. This implies the Zn^{2+} may be able to attract as many as AN molecules in the solution up to the limit, i.e. all Zn^{2+} forms the $Zn(AN)_6^{2+}$ complex. Interestingly, by composing the pseudo-phase diagram of the $Zn(H_2O)_x(AN)_{6-x}^{2+}$ complexes as shown in Figure 1b, all of the possible x is characterized by a convex hull. Therefore, no tendency of phase separation to form specific types of complexes should be expected.

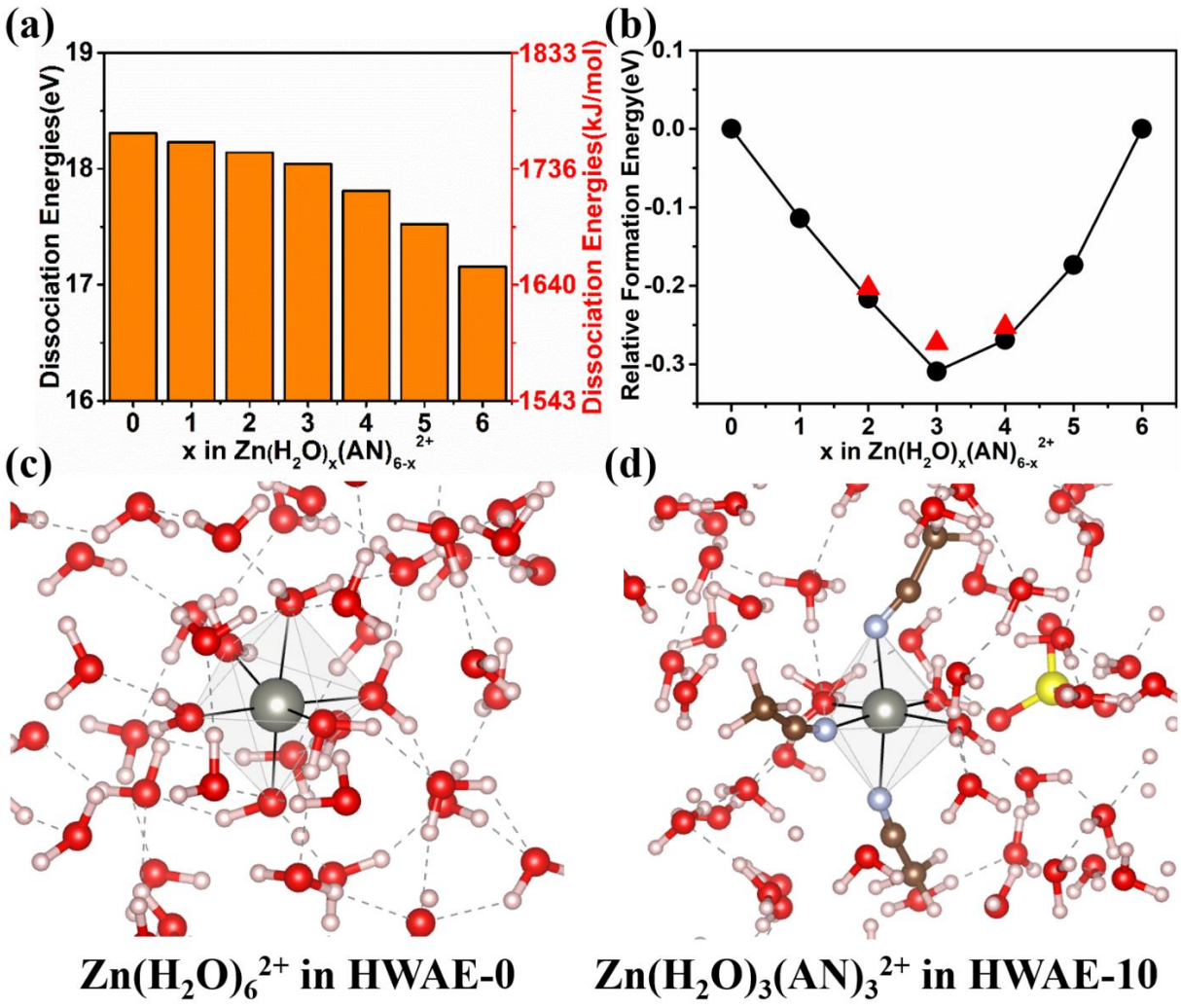

Figure 1. (a) Dissociation energies of the $Zn(H_2O)_x(AN)_{6-x}^{2+}$ complexes; (b) Pseudo phase diagram of $Zn(H_2O)_x(AN)_{6-x}^{2+}$. The black dots and the red triangles represent the most stable and the unstable configurations of the complexes, respectively; Snapshots of the AIMD simulations of (c) HWAE-0 and (d) HWAE-10 (another two types of stably existing solvation complexes in HWAE-10 are shown in supporting information).

The above results give strong implications on the change of the solvation structure of Zn^{2+} when AN is incorporated in the electrolyte. However, such calculations are carried out in their gas phases, and only the first solvation sheath is considered, as shown in Figure S3. Therefore, they cannot fully reflect the microscopic features of the electrolytes in their liquid phases. To further evaluate the solvation structure of the electrolyte and the stability of the solvation complexes as discussed above, *ab-initio* molecular dynamics (AIMD) simulations are carried

out on two typical electrolytes, i.e., HWAE-0 in water and the HWAE-10. We found that in HWAE-0, $Zn(H_2O)_6^{2+}$ is stable during the entire simulation period (Figure 1c), in agreement with previous reports. In sharp contrast, such a complex tends to decompose in HWAE-10 while another three types of solvation complexes can stably exist in HWAE-10 during the 100 ps of AIMD simulations at 300 K, which are $Zn(H_2O)_5(AN)_1^{2+}$, $Zn(H_2O)_4(AN)_2^{2+}$, and $Zn(H_2O)_3(AN)_3^{2+}$ (see Figures 1d and S4 for snapshots). Therefore, in HWAE-10, the ANs are expected to be able to replace up to 3 water molecules in the $Zn(H_2O)_6^{2+}$ complex and significantly change the desolvation dynamics of Zn^{2+}, thereby influencing the electrodeposition behavior of Zn metal.

To explore the effect of solvation structure on Zn deposition and stripping process, cyclic voltammetry (CV) is conducted using a three-electrode cell in 0.1 M $ZnSO_4$ electrolyte with/without AN. Low concentrated electrolyte is selected to clearly present the reduction peaks.[42] Glassy carbon is employed as a working electrode, and platinum plate and saturated calomel electrode (SCE) serve respectively as the counter and the reference electrode. As shown in **Figures 2**a, S5 and Tables S1, the reduction potential is -1.45 V in 0.1 M $ZnSO_4$ electrolyte, which gradually shifts to a more negative potential with an increasing amount of AN in the solvent, reaching -1.53 V in 0.1 M $ZnSO_4$ with 15% AN. The voltage profiles during deposition and stripping are obtained using a three-electrode cell with Zn foils as the working/counter/reference electrodes. The test condition and the configuration of such three-electrode are close to the practical cell while avoiding the interference of the counter electrode. A higher nucleation overpotential and voltage potential are observed with AN addition (Figure S6). The value of nucleation overpotential reflects the energy barrier of heterogeneous nucleation during initial deposition, which is defined as the difference between the voltage tip and the stable voltage platform.[43] The combined CV and voltage profile results indicate a larger potential polarization is required to realize the nucleation and the following growth of Zn in hybrid water/AN electrolytes. The nucleation overpotential is further evaluated using Zn/Cu

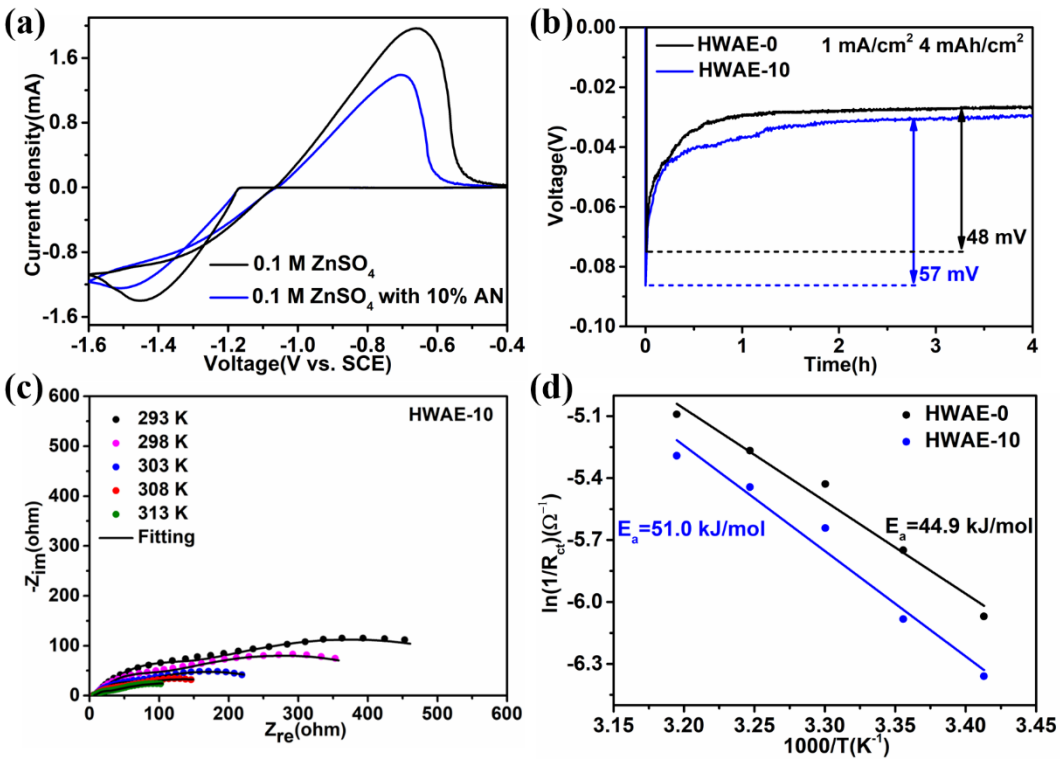

Figure 2. (a) CV at a scan rate of 20 mV/s in 0.1 M $ZnSO_4$ and 0.1 M $ZnSO_4$ with 10% AN; (b) Nucleation overpotentials using Zn/Cu cells in HWAE-0 and HWAE-10; (c) Nyquist plots at different temperatures using Zn/Cu cells in HWAE-10; (d) The activation energies obtained from Nyquist plots using Zn/Cu cells in HWAE-0 and HWAE-10.

coin cells, where Cu foil serves as the working electrode, and Zn foil is employed as the counter/reference electrode. As shown in Figures 2b and S7, similar behavior is also observed in Zn/Cu cells. The nucleation overpotential increases from 48 mV in the electrolyte with neat H_2O solvent to 52, 57, and 60 mV when 5%, 10%, and 15% AN is incorporated as a co-solvent, respectively. To quantitatively compare the desolvation barrier during Zn^{2+} deposition, EIS at different temperatures is conducted in the two typical electrolytes, i.e., HWAE-0 and HWAE-10 (Figures 2c and S8). The experimental data is fitted using an equivalent circuit shown in Figure S9. The activation energy (E_a) is calculated based on the Arrhenius equation:

$$1/R_{ct}=Aexp(-E_a/RT)$$

where R_{ct} is the charge transfer resistance, A is the pre-exponential constant, T is the absolute temperature, and R is the standard gas constant. As shown in Figure 2d, the activation energy in HWAE-0 is 44.9 kJ/mol, while HWAE-10 presents a higher value of 51.0 kJ/mol. The result is consistent with the larger desolvation energy barrier in hybrid water/AN electrolytes as suggested by the theoretical calculations.

The high overpotential associated with strong solvation in the hybrid electrolytes would lead to supersaturating of Zn atoms adsorption on the surface, which gives rise to increased nucleation size and smooth Zn deposition.[24,44] In the absence of AN, only few adatoms are presented and turn into Zn nuclei on the surface of Cu current collector owing to the low desolvation energy required for $Zn(H_2O)_6^{2+}$. The Zn atoms then continuously deposit on the existed sparse Zn nuclei, eventually causing the preferential Zn dendrites growth as schematically shown in **Figure 3**a. On the contrary, supersaturation of adatoms are accumulated between the electrode/electrolyte interfaces arising from the high nucleation overpotential under the HWAE-10 system. Thus, numerous Zn nuclei will be produced for the homogenous Zn growth.

The above assumption is fully supported by the SEM images taken at various stages. We monitor the Zn growth process by collecting the electrodes from initial deposition to after repeated cycles, as shown in Figures 3b and 3c. To examine the early nucleation behavior, a tiny amount Zn of 0.0002 mAh/cm^2 (corresponding to 0.72 s deposition time) is deposited on Cu current collector. Sparse Zn nucleation with plate-like morphology is observed in HWAE-0. The Zn clusters gradually cover the surface of Cu with an increased Zn deposition amount of 0.005 mAh/cm^2 and 0.2 mAh/cm^2, but the plate-like structure is maintained and randomly oriented. Also, huge protuberances and tiny flakes with sharp tips are detected (Figure S10). With an increased deposition capacity of 1 mAh/cm^2 and 4 mAh/cm^2, deteriorative morphologies with the formation of porous microstructure and vast huge flakes are observed (Figure S11). After 50 cycles, the Zn metal presents a looser and rougher structure with the

larger flakes. These microsized flakes with sharp tips would easily trigger the internal short circuit when they continue to grow. By contrast, the AN addition enables highly improved Zn

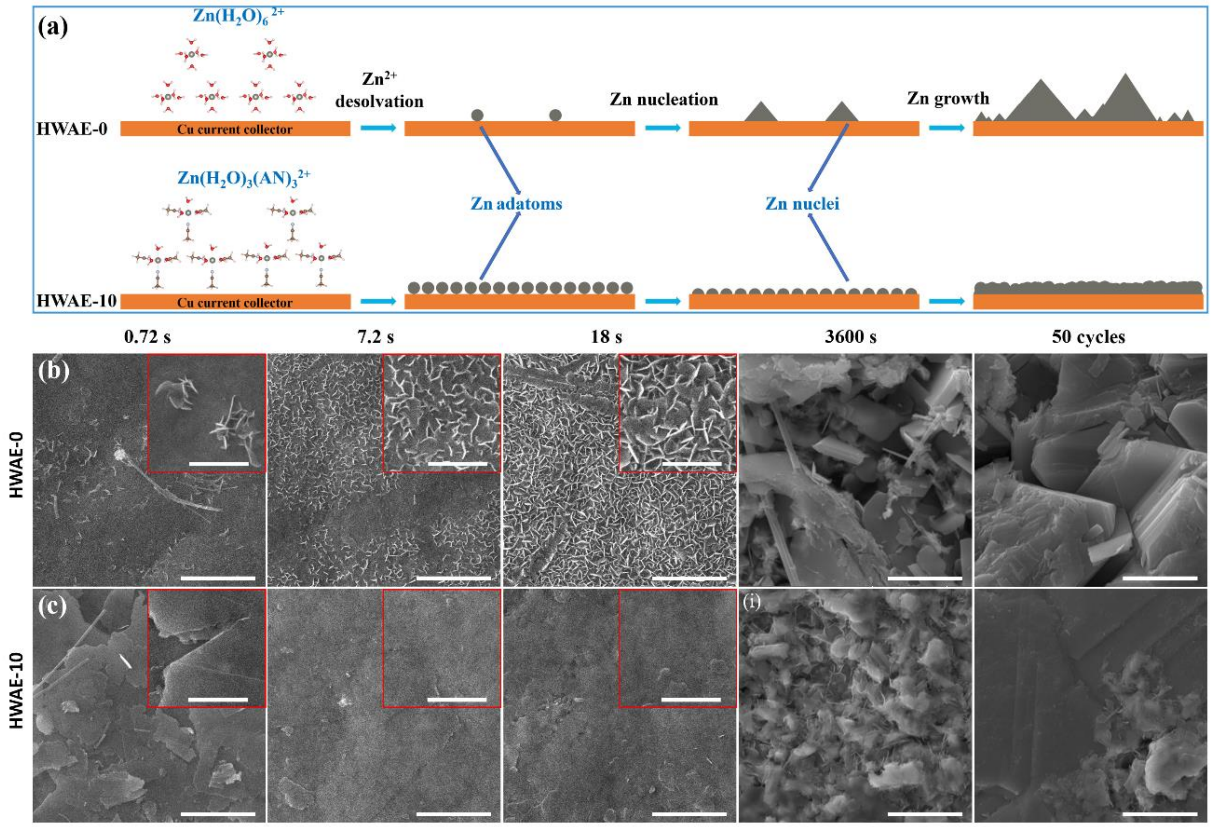

Figure 3. (a) Schematic illustration of the Zn nucleation and growth process in HWAE-0 and HWAE-10; SEM images of Zn deposited on Cu current collector at 1 mA/cm^2 with various amount of 0.0002 mAh/cm^2 (0.72 s), 0.002 mAh/cm^2 (7.2 s), 0.005 mAh/cm^2 (18 s), and 1 mAh/cm^2 (3600 s) and after 50 cycles at 2 mA/cm^2 with a cycling capacity of 2 mAh/cm^2 in HWAE-0 (b) and HWAE-10 (c). The scale bars in figures and insets represent 5 μm and 2 μm, respectively.

deposition behavior and leads to massive nucleation sites under the capacity of 0.0002 mAh/cm^2. Flat Zn plates that parallel to the Cu current collector is presented. The oriented Zn growth in HWAE-10 is similar to the previous reported epitaxial Zn electrodeposition to some extent[45], helping to realize highly reversible Zn deposition/stripping. The Zn gradually cover the Cu current collector with increasing deposition capacities (Figure S11), while maintaining the smooth surface. It is worth mentioning that the Zn deposition remains a homogenous and

compact surface after 50 cycles in HWAE-10. It demonstrates the superior reversibility of the deposition/stripping process in HWAE-10. The optical photos of these electrodes after Zn plating in HWAE-0 and HWAE-10 also support these findings (Figure S12). Zn is randomly deposited, and only partial Cu current collector is coated in HWAE-0, because of the preferential growth of Zn on the "hot spot". Turn to the case in HWAE-10, Cu current collector is evenly covered with the deposited Zn. Therefore, the AN co-solvent could regulate the Zn deposition/stripping behavior for obtaining a smooth and dense structure, which shows distinct characteristics with the rough and loose morphology formed in HWAE-0.

The smooth deposition of Zn in the hybrid H_2O/AN solvents, due to the strong solvation sheath, would help to improve the cycling and CE performances. It is well known that cycling performances are highly related to the depth of discharge (DOD). To verify the effectiveness of hybrid water/AN electrolytes, a rigorous DOD of 50% is selected to study the cycling life in Zn/Cu cells. Specifically, 4 mAh/cm^2 of Zn is firstly deposited onto Cu current collector at 1 mA/cm^2, and a fixed cycling capacity of 2 mAh/cm^2 is adopted under various current densities. At 0.5 mA/cm^2, the Zn/Cu cell suffers from the short circuit after ~500 h cycling in HWAE-0 (Figure S13). With the incorporation of AN, much-improved performances are achieved, and the cycling life prolongs as the amount of AN increases. Zn/Cu cells deliver stable cycling of ~530 h, ~870 h, and ~1000 h in HWAE-5, HWAE-10, and HWAE-15, respectively. The same trends persist when the current densities are increased to 1 and 2 mA/cm^2. Zn/Cu cells experience short circuits at ~290 h at 1 mA/cm^2 and fail at ~120 h at 2 mA/cm^2 in HWAE-0 (**Figures 4**a and 4b). On the contrary, prolonged cycling life of ~580 h and ~700 h are realized at 1 mA/cm^2 in HWAE-10 and HWAE-15, respectively. Even at 2 mA/cm^2, Zn/Cu cells still display stable voltage profiles for ~570 h and ~650 h in HWAE-10 and HWAE-15, respectively. Noteworthy, the short circuit accounts for the failure of Zn/Cu cells at 0.5 and 1 mA/cm^2 in HWAE-0, while the increased voltage polarization is responsible for the degradation in HWAE-10 and HWAE-15. It is speculated the smooth Zn deposition in the electrolyte with hybrid

solvents effectively inhibits the dendrite growth during the long-term cycles. This is confirmed by the morphology of Zn after 200 cycles (400 h) at 2 mA/cm^2 in HWAE-10. The Zn deposition maintains a compact and uniform structure without dendrites growth, as shown in Figure S14.

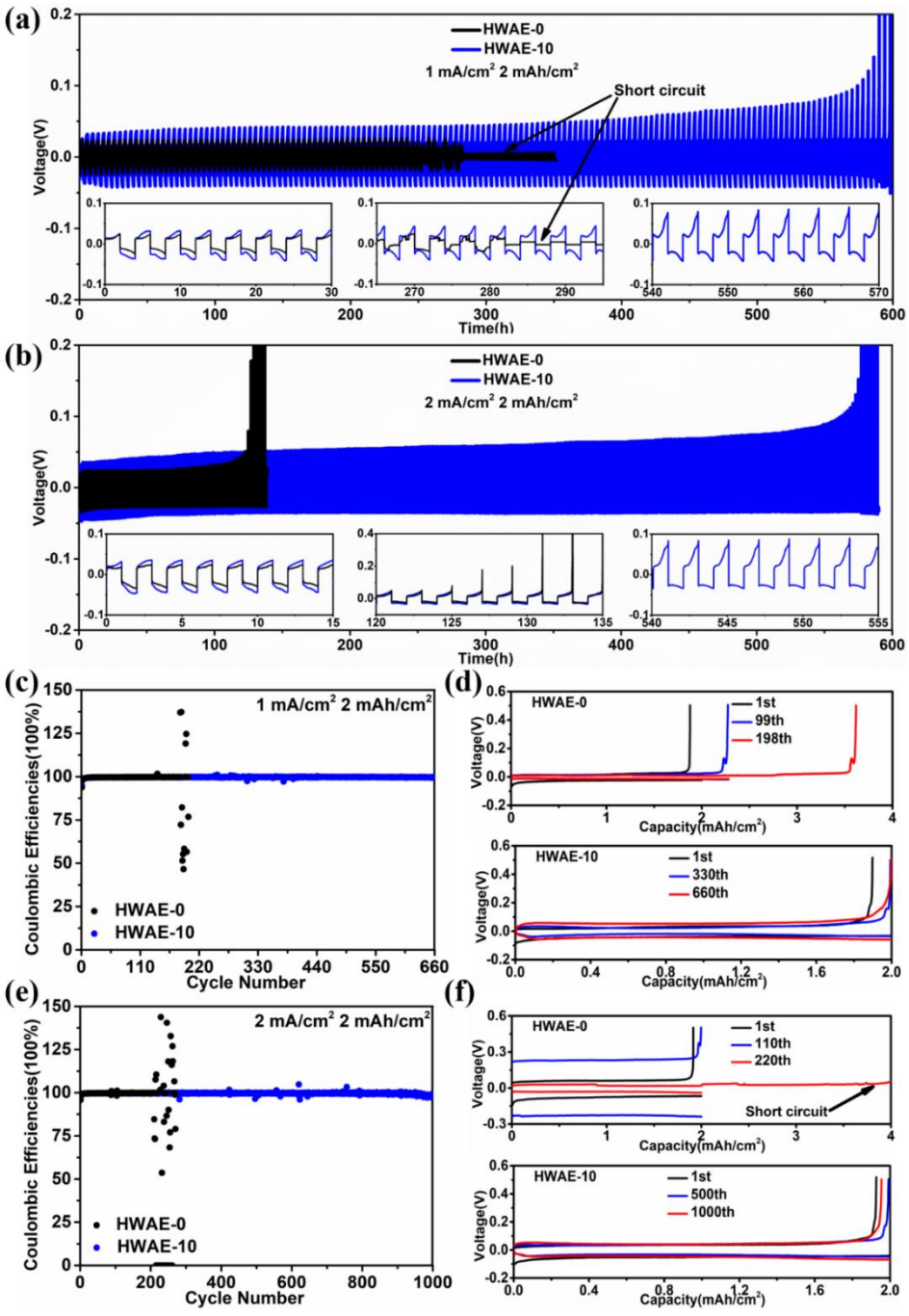

Figure 4. The cycling performances of Zn/Cu cells in HWAE-0 and HWAE-10 at (a) 1 mA/cm^2, (b) 2 mA/cm^2 with a cycling capacity of 2 mAh/cm^2 (corresponds to 50% DOD); CEs of Zn/Cu cells in HWAE-0 and HWAE-10 at (c) 1 mA/cm^2 and (e) 2 mA/cm^2 with a cycling capacity of

2 mAh/cm^2; Detailed deposition/stripping voltage curves in HWAE-0 and HWAE-10 at (d) 1 mA/cm^2 and (f) 2 mA/cm^2 with a cycling capacity of 2 mAh/cm^2.

CE is another critical parameter to evaluate the reversibility of Zn deposition/stripping. The CE of Zn/Cu cells is measured at 1 mA/cm^2 and 2 mA/cm^2 with fixed cycling capacity of 2 mAh/cm^2. The cell starts to oscillate drastically after 190 and 210 cycles at 1 mA/cm^2 and 2 mA/cm^2 in HWAE-0 (Figures 4c and 4e). The inferior performance is ascribed to the formation of Zn dendrites with large surface area upon repeated cycles, promoting the severe parasitic reactions.[19, 28] Moreover, the polarization increases with cycling, and short circuit occurs ultimately in HWAE-0, as shown Figures 4d, 4f and S15. In contrast, Zn/Cu cells present a highly improved CE performance in hybrid water/AN electrolytes due to ameliorative Zn deposition/stripping behavior. Among hybrid water/AN electrolytes, Zn/Cu cells deliver the best CE performances in HWAE-10, followed by HWAE-15 and HWAE-5 (Figure S16-S19). The cell shows a high average CE of 99.65 % for 660 cycles (2640 h) at 1 mA/cm^2 in HWAE-10. When the current density increases to 2 mA/cm^2, it still services for 1000 cycles (2000 h) with an average CE of 99.64 %. From the time-voltage curves and corresponding detailed deposition/stripping voltage curve, Zn/Cu cells present stable voltage curves for each cycle. The inferior CE performances in HWAE-5 are attributed to inadequate complexation between less AN and Zn^{2+}, and thus the Zn deposition is not regulated sufficiently. As for HWAE-15, excessive AN addition leads to the highly hampered deposition behavior, probably facilitating the side reaction, such as hydrogen evolution reaction (HER). Notably, the cycling performance in HWAE-15 is better than that in HWAE-10, while the CE performance results are opposite. The reason lies in the effective suppression of HER arising from the presence of Zn during cycling test. HER is more likely to occur on Cu metal than Zn metal.[46,47] Zn^{2+} is directly deposited on the bare surface of Cu current collector under CE test, leading to the worse CE performance of HWAE-15 than HWAE-10.

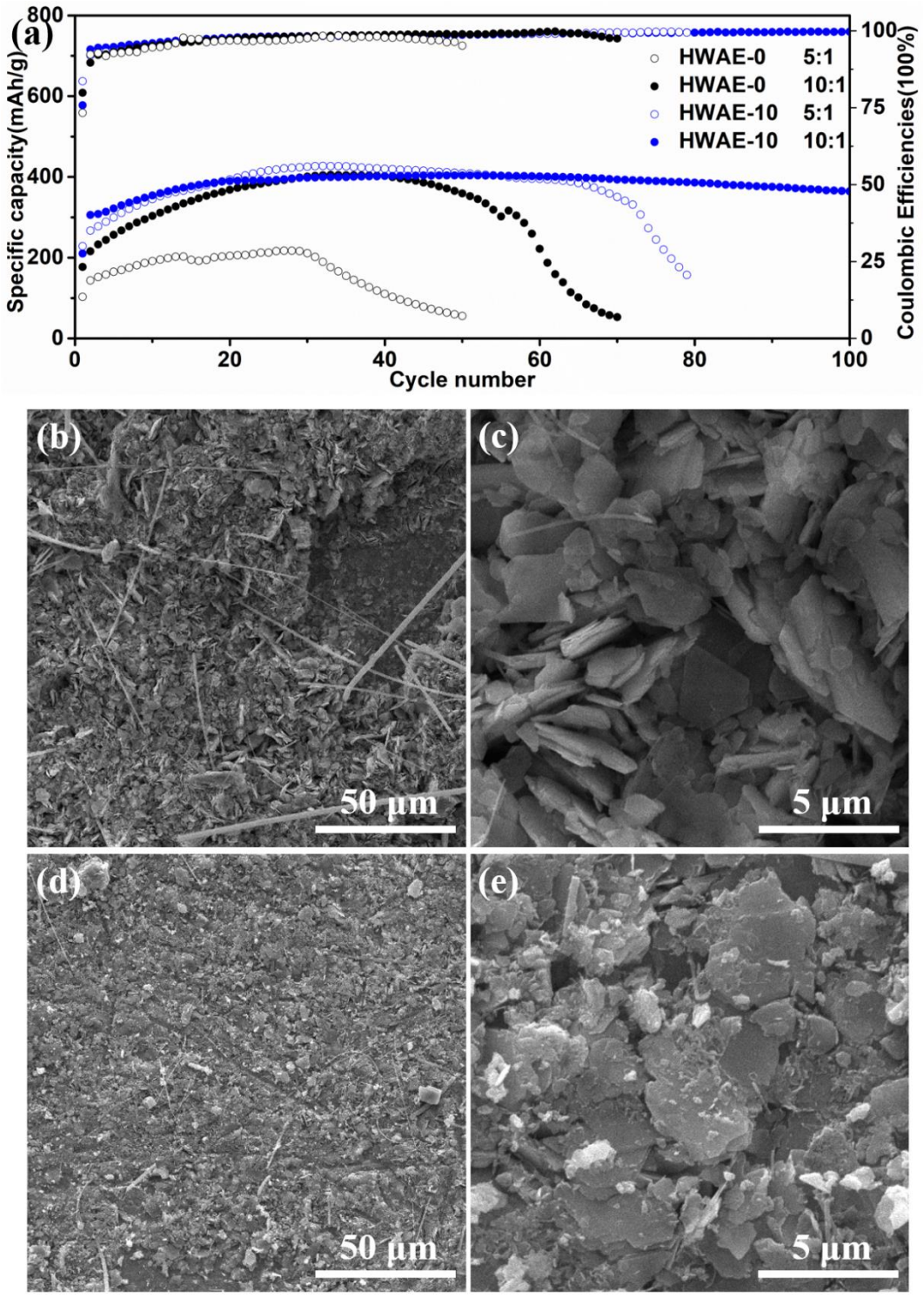

Figure 5. (a) Cycle performances of Zn/MnO_2 batteries at 300 mA/g in HWAE-0 and HWAE-10, with N:P ratios of 5:1 and 10:1; Corresponding SEM images of Zn after 70 cycles in (c, d) HWAE-0 and after 150 cycles in (e, f) HWAE-10, with N:P ratio of 10:1.

To assess the performance of HWAE-10 under practical conditions, the full cells coupling with a MnO_2 cathode are assembled. Cu foil with pre-deposited Zn is used as an anode, and the

negative-to-positive electrode capacity (N:P) ratios are set to 5:1 and 10:1, respectively. With N:P ratios of 5:1 and 10:1, the discharge capacity of MnO_2 dramatically decreases after ~30 cycles and ~50 cycles in HWAE-0, indicating the poor reversibility of Zn metal (**Figure 5**a). On the contrary, AN addition enables an improved cycle life and realize a stable capacity for ~70 cycles (N:P = 5:1). With the N:P ratio of 10:1, the cell maintains capacity retention of ~90% over 100 cycles in HWAE-10, which is significantly superior to that in HWAE-0. The stable cycling performance of the full cells verifies the compatibility of AN additive to the cathode. Another issue associated with the presence of an organic solvent is safety. It is a delight to find that the HAWE-10 remains non-flammable and thus maintain the safety nature of aqueous battery systems (Figure S20). The SEM images of the cycled anode are examined to further validate the improved stability in full cells. The Zn metal shows rough and loose structures after 70 cycles in HWAE-0 (Figure 5b and 5c), while the much smooth textures are observed after 150 cycles in HWAE-10 (Figure 5d and 5e). These results are consistent with the enhanced lifespan of symmetrical Zn cells and verify the potential application toward full cells.

3. CONCLUSIONS

In the electrodeposition industry, complexing agents are commonly employed as brighteners to regulate the solvation structure of metal ion for achieving smooth coating. Motivated by this mechanism, we manipulate the solvation structure of Zn^{2+} through the adoption of AN as a co-solvent in the electrolyte. Both experiments and simulations results suggest that the AN incorporation alters the solvation sheath by replacement of a portion of water that surrounds Zn^{2+}. This unique solvation structure elevates the nucleation overpotential for improving the deposition sites, which results in compact and uniform Zn growth. Therefore, a stable Zn deposition/stripping performance up to ~650 h at 2 mA/cm^2 with 50% DOD is achieved, which is more than five-fold longer than that without complexing agent under the same test condition.

Moreover, Zn/Cu cells demonstrate a high CE of 99.64% on average over 1000 cycles (equals to 2000 h) in HWAE-10 at 2 mA/cm^2 under cycling capacity of 2 mAh/cm^2. The compatibility of the mixed solvent with the cathode is verified by Zn/MnO_2 full-cell examination, which shows excellent cyclic stability even with a limited excess of Zn metal on the anode side. This work opens a viable route to stabilize Zn metal anode by optimizing the solvation structure of Zn^{2+}.

4. Experimental Section

Material Synthesis: MnO_2 is fabricated by the traditional hydrothermal method based on the previous report.[48] 0.507 g $MnSO_4 \cdot H_2O$ and 2 ml H_2SO_4 (0.5 M) were added into 90 ml deionized water and magnetically stirred until it turned to transparent. The 20 ml $KMnO_4$ (0.1 M) solution was added into the solution dropwise, followed by stirring for 2 h. The mixture was then loaded into Teflon-lined autoclave and heated at 120 ℃ for 12 h. The solution was centrifuged three times, which was then dried under vacuum oven at room temperature to obtain the final product.

Characterizations: The electrodes dissembled from the cycled cells were washed with deionized water for two times to remove the residual salts. The scanning electron microscope (SEM) images and the roughness of these dried electrodes were then recorded by Tescan VEGA3 and the atomic force microscope (AFM, Brucker), respectively. Infrared spectra (IR) were collected using a Shimadzu Fourier transform infrared spectrometer.

Electrochemical measurements: CR2032 coin-type cells were assembled using the glass fiber (Whatman, GF/D) as separator and Cu foil as the working electrode. A piece of zinc metal is adopted as both a counter and reference electrode to make a Zn/Cu cell. 1 M $ZnSO_4$ in water and hybrid water/acetonitrile were used as electrolytes. A volume ratio of water to acetonitrile is controlled to be 95:5, 90:10, 85:15. These hybrid water/acetonitrile electrolytes are denoted as HWAE-X, where “X” represents the volume proportion of acetonitrile. HWAE-0 denotes 1

M $ZnSO_4$ in water without the addition of AN. The CE was evaluated using Zn/Cu cells at 1 or 2 mA/cm^2 with a fixed deposition capacity of 2 mAh/cm^2, and a charge cutoff voltage is 0.5 V. CE was calculated based on the capacity ratio of stripping to deposition. For cycling performance, 4 mAh/cm^2 of Zn was firstly deposited onto Cu current collector at a current density of 1 mA/cm^2. A 50% depth of discharge (DOD), corresponding to 2 mAh/cm^2 of Zn, was used to cycle at various current densities of 0.5, 1 and 2 mA/cm^2. The cyclic voltammetry (CV) measurements were carried out on a Princeton (Parstat 4000) electrochemical station using a beaker-type three-electrode cell, where glassy carbon is employed as working electrode, and a platinum plate and saturated calomel electrode (SCE) serve respectively as the counter and the reference electrode. Electrochemical impedance spectroscopy (EIS) was performed by BioLogic electrochemical workstation (VSP) from 10^5 Hz and 10^{-1} Hz at the potential amplitude of 5 mV. A cathode consisting of 70% MnO_2, 20% Super P and 10% PVDF is coupled with the anode for full cell evaluation. A certain amount of Zn was pre-deposited on Cu foil with a negative-to-positive electrode capacity (N:P) ratio varying from 5:1 or 10:1 to prepare the anode. 0.1 M $MnSO_4$ were added to HWAE-0 and HWAE-10 to suppress the dissolution of Mn^{2+} from the cathode.[48] The full cells were cycled at 300 mA/g between 0.8 and 1.9 V.

Theoretical Computations: The quantum chemical computations for small molecules and clusters were carried out using ORCA on the level of density functional theory (DFT).[49] The B3LYP hybrid functional was adopted, and the correlation-consistent polarization plus valence double-ζ (cc-pVDZ) basis set of Dunning was used during the electron self-consistency.[50-52] The coordination number of Zn^{2+} was selected as 6 according to previous theoretical and experimental studies.[53,54] Due to the octahedrally coordinated nature of Zn^{2+}, 2 possible configurations are possible for $Zn(H_2O)_x(AN)_{6-x}^{2+}$ (x=2,3,4), leading to a total number of 9 configurations for all possible x. The dissociation energy E_d of the complexes were calculated by

$$E_d(x) = E_{Zn^{2+}} + (6-x)E_{water} + xE_{AN} - E_{Zn(H_2O)_x(AN)_{6-x}{}^{2+}}, \qquad (x = 0,1,2,3,4,5,6)$$

where $E_{Zn^{2+}}$, E_{water}, E_{AN}, and $E_{Zn(H_2O)_x(AN)_{6-x}{}^{2+}}$ are the total energies of the Zn^{2+} cation, the water molecule, the AN molecule, and the $Zn(H_2O)_x(AN)_{6-x}{}^{2+}$ complexes in the gas phases, respectively.

The relative formation energies of $Zn(H_2O)_x(AN)_{6-x}{}^{2+}$ are calculated by

$$E_f(x) = -E_d(x) + [(6-x)E_d(0) + xE_d(6)]/6, \qquad (x = 0,1,2,3,4,5,6)$$

The ab-initio molecular dynamics simulations (AIMD) were carried out for two representative electrolytes, i.e., HWAE-0 and HWAE-10 under the Born-Oppenheimer approximation.[55,56] The computational setup of the periodic DFT was consistent with the materials project as well as our previous work.[57-64] Briefly, the generalized gradient approximation (GGA) with the Perdew-Burke-Ernzerhof (PBE) functional was adopted.[65] For the self-consistent electron calculations, the energy cutoff of plane waves was set at 400 eV. Projector Augmented Wave (PAW) method was used to model the core electrons.[66] The Brillouin zone was sampled at the Γ point. An energy convergence criterion of 10^{-4} eV was set for the electron self-consistent calculations. The temperature was controlled at 300 K using a Nose-Hoover thermostat with a fixed simulation box size (NVT ensemble).[67] The time step was chosen to be 0.5 fs. The simulation length was set to 100 ps. The simulation boxes for the HWAE-0 electrolyte were constructed so that it contains 51 water molecules, 1 $Zn(H_2O)_6{}^{2+}$, and 1 $SO_4{}^{2+}$. The side lengths of the simulation boxes were chosen so that the density of the system is 1.2 g/cm^3. For the HWAE-10 electrolyte, three simulation boxes were created for four separate AIMD runs. In each simulation box, 39+x water molecules, 1 Zn $(AN)_x(H_2O)_{6-x}{}^{2+}$, 3-x AN, and 1 $SO_4{}^{2+}$ were included (x=0,1,2,3). For each box, 100 ps of simulations were carried out.

Supporting Information

Supporting Information is available from the Wiley Online Library or from the author.

Acknowledgements

This work was financially supported by the Research Grant Council of Hong Kong (GRF project: 15305219), the Basic Research Program of Shenzhen (No. JCYJ20190812161409163), the Basic and Applied Basic Research Program of Guangdong Province (No. 2019A1515110531), the SIAT Innovation Program for Excellent Young Researchers

Received: ((will be filled in by the editorial staff))
Revised: ((will be filled in by the editorial staff))
Published online: ((will be filled in by the editorial staff))

References

[1] J. M. Tarascon, M. Armand, *Nature* **2001**, *414*, 359.
[2] M. Li, J. Lu, Z. Chen, K. Amine, *Adv. Mater.* **2018**, *30*, 1800561.
[3] D. Larcher, J. M. Tarascon, *Nat. Chem.* **2015**, *7*, 19.
[4] L. E. Blanc, D. Kundu, L. F. Nazar, *Joule* **2020**, *4*, 771.
[5] H. Li, L. Ma, C. Han, Z. Wang, Z. Liu, Z. Tang, C. Zhi, *Nano Energy* **2019**, *62*, 550.
[6] X. Zeng, J. Hao, Z. Wang, J. Mao, Z. Guo, *Energy Storage Mater.* **2019**, *20*, 410.
[7] M. Song, H. Tan, D. Chao, H. J. Fan, *Adv. Funct. Mater.* **2018**, *28*, 1802564.
[8] Q. Zhang, J. Luan, Y. Tang, X. Ji, H. Y. Wang, *Angew. Chem. Int. Ed.* **2020**, DOI: 10.1002/anie.202000162.
[9] J. Q. Huang, X. Lin, H. Tan, X. Du, B. Zhang, *J. Energy Chem.* **2020**, *43*, 1.
[10] Q. Yang, G. Liang, Y. Guo, Z. Liu, B. Yan, D. Wang, Z. Huang, X. Li, J. Fan, C. Zhi, *Adv. Mater.* **2019**, *31*, 1903778.
[11] A. Naveed, H. Yang, J. Yang, Y. Nuli, J. Wang, *Angew. Chem. Int. Ed.* **2019**, *58*, 2760.
[12] Q. Zhang, J. Luan, L. Fu, S. Wu, Y. Tang, X. Ji, H. Wang, *Angew. Chem. Int. Ed.* **2019**, 58, 15841.
[13] Y. Zeng, X. Zhang, R. Qin, X. Liu, P. Fang, D. Zheng, Y. Tong, X. Lu, *Adv. Mater.* **2019**, *31*, 1903675.
[14] Y. Yin, S. Wang, Q. Zhang, Y. Song, N. Chang, Y. Pan, H. Zhang, X. Li, *Adv. Mater.* **2020**, *32*, 1906803.
[15] X. Xie, S. Liang, J. Gao, S. Guo, J. Guo, C. Wang, G. Xu, X. Wu, G. Chen, J. Zhou, *Energy Environ. Sci.* **2020**, *13*, 503.
[16] Q. Guan, Y. Li, X. Bi, J. Yang, J. Zhou, X. Li, J. Cheng, Z. Wang, B. Wang, J. Lu, *Adv. Energy Mater.* **2019**, *9*, 1970163.
[17] W. Xu, K. Zhao, W. Huo, Y. Wang, G. Yao, X. Gu, H. Cheng, L. Mai, C. Hu, X. Wang, *Nano Energy* **2019**, *62*, 275.
[18] J. Zhao, J. Zhang, W. Yang, B. Chen, Z. Zhao, H. Qiu, S. Dong, X. Zhou, G. Cui, L. Chen, *Nano Energy* **2019**, *57*, 625.
[19] H. Qiu, X. Du, J. Zhao, Y. Wang, J. Ju, Z. Chen, Z. Hu, D. Yan, X. Zhou, G. Cui, *Nat. Commun.* **2019**, *10*, 5374.
[20] K. E. Sun, T. K. Hoang, T. N. Doan, Y. Yu, X. Zhu, Y. Tian, P. Chen, *ACS Appl. Mater. Interfaces* **2017**, *9*, 9681.
[21] J. Q. Huang, X. Guo, X. Lin, Y. Zhu, B. Zhang, *Research* **2019**, *2019*, 2635310.
[22] C. Deng, X. Xie, J. Han, Y. Tang, J. Gao, C. Liu, X. Shi, J. Zhou, S. Liang, *Adv. Funct. Mater.* **2020**, *30*, 2000599
[23] K. Zhao, C. Wang, Y. Yu, M. Yan, Q. Wei, P. He, Y. Dong, Z. Zhang, X. Wang, L. Mai, *Adv. Mater. Interfaces* **2018**, *5*, 1800848.
[24] Z. Zhao, J. Zhao, Z. Hu, J. Li, J. Li, Y. Zhang, C. Wang, G. Cui, *Energy Environ. Sci.* **2019**, *12*, 1938.
[25] P. Liang, J. Yi, X. Liu, K. Wu, Z. Wang, J. Cui, Y. Liu, Y. Wang, Y. Xia, J. Zhang, *Adv. Funct. Mater.* **2020**, *30*, 1908528.

[26] T. Franklin, *Surf. Coat. Technol.* **1987**, *30*, 415.
[27] F. Wang, O. Borodin, T. Gao, X. Fan, W. Sun, F. Han, A. Faraone, J. A. Dura, K. Xu, C. Wang, *Nat. Mater.* **2018**, *17*, 543.
[28] C. Y. Chen, K. Matsumoto, K. Kubota, R. Hagiwara, Q. Xu, *Adv. Energy Mater.* **2019**, *9*, 1970086.
[29] D. Sobha Jayakrishnan, *Corrosion Protection and Control Using Nanomaterials*, **2012**, pp. 86.
[30] G. Wilcox, P. Mitchell, *J. Power Sources* **1989**, *28*, 345.
[31] Z. Mahmud, G. Gordillo, L. Gassa, C. Ventura D'Alkaine, Universidad de Buenos Aires. Facultad de Ciencias Exactas y Naturales, **2016**.
[32] M. S. Chandrasekar, S. Srinivasan, M. Pushpavanam, *J. Mater. Sci.* **2009**, *45*, 1160.
[33] M. C. Li, L. L. Jiang, W. Q. Zhang, Y. H. Qian, S. Z. Luo, J. N. Shen, *J. Solid State Electrochem.* **2006**, *11*, 549.
[34] C. Loto, *Asian J. Appl. Sci.* **2012**, *5*, 314.
[35] M. Schwartz, *Handbook of Deposition Technologies for Films and Coatings—Science, Technology and Applications* **1994**, pp, 506.
[36] B. Intertec, St. Paul, MN: Minnesota Office of Waste Management, **1992**.
[37] S. Anwar, Y. Zhang, F. Khan, *RSC Adv.* **2018**, *8*, 28861.
[38] Y. Marcus, *J. Phys. Org. Chem.* **2012**, *25*, 1072.
[39] J. E. Bertie, Z. Lan, *J. Phys. Chem. B* **1997**, *101*, 4111.
[40] T. E. Cooper, D. Carl, P. Armentrout, *J. Phys. Chem. A* **2009**, *113*, 13727.
[41] K. Waizumi, H. Ohtaki, H. Masuda, N. Fukushima, Y. Watanabe, *Chem. Lett.* **1992**, *21*, 1489.
[42] P. Kissinger, W. R. Heineman, *Laboratory Techniques in Electroanalytical Chemistry, revised and expanded*, CRC press, **2018**, pp.
[43] Z. Hou, Y. Yu, W. Wang, X. Zhao, Q. Di, Q. Chen, W. Chen, Y. Liu, Z. Quan, *ACS Appl. Mater. Interfaces* **2019**, *11*, 8148.
[44] J. Dong, H. Dai, Q. Fan, C. Lai, S. Zhang, *Nano Energy* **2019**, *66*, 104128.
[45] J. Zheng, Q. Zhao, T. Tang, J. Yin, C. D. Quilty, G. D. Renderos, X. Liu, Y. Deng, L. Wang, D. C. Bock, C. Jaye, D. Zhang, E. S. Takeuchi, K. J. Takeuchi, A. C. Marschilok, L. A. Archer, *Science* **2019**, *366*, 645.
[46] X. G. Zhang, *Corrosion and Electrochemistry of Zinc*, Springer Science & Business Media, **2013**, pp.
[47] J. Du, J. Wang, L. Ji, X. Xu, Z. Chen, *ACS Appl. Mater. Interfaces* **2016**, *8*, 30205.
[48] H. Pan, Y. Shao, P. Yan, Y. Cheng, K. S. Han, Z. Nie, C. Wang, J. Yang, X. Li, P. Bhattacharya, K. T. Mueller, J. Liu, *Nature Energy* **2016**, *1*, 16039.
[49] F. Neese, *Wiley Interdiscip. Rev. Comput. Mol. Sci.* **2012**, *2*, 73.
[50] A. D. Becke, *J. Chem. Phys.* **1993**, *98*, 1372.
[51] P. J. Stephens, F. Devlin, C. Chabalowski, M. J. Frisch, *J. Phys. Chem.* **1994**, *98*, 11623.
[52] T. H. Dunning Jr, *J. Chem. Phys* **1989**, *90*, 1007.
[53] P. D'Angelo, V. Migliorati, *J. Phys. Chem. B* **2015**, *119*, 4061.
[54] M. Arab, D. Bougeard, K. Smirnov, *Chem. Phys. Lett.* **2003**, *379*, 268.
[55] J. Hafner, *J. Comput. Chem.* **2008**, *29*, 2044.
[56] G. Kresse, J. Hafner, *Phys. Rev. B* **1993**, *47*, 558.
[57] A. Jain, S. P. Ong, G. Hautier, W. Chen, W. D. Richards, S. Dacek, S. Cholia, D. Gunter, D. Skinner, G. Ceder, *Apl. Mater.* **2013**, *1*, 011002.
[58] S. P. Ong, W. D. Richards, A. Jain, G. Hautier, M. Kocher, S. Cholia, D. Gunter, V. L. Chevrier, K. A. Persson, G. Ceder, *Comp. Mater. Sci.* **2013**, *68*, 314.
[59] Z. Lu, J. Liu, F. Ciucci, *Energy Storage Mater.* **2020**, *28*, 146
[60] J. Yi, J. Chen, Z. Yang, Y. Dai, W. Li, J. Cui, F. Ciucci, Z. Lu, C. Yang, *Adv. Energy Mater.* **2019**, *9*, 1901796.

[61] Z. Lu, F. Ciucci, *J. Mater. Chem. A* **2018**, *6*, 5185.
[62] Z. Lu, F. Ciucci, *Chem. Mater.* **2017**, *29*, 9308.
[63] Z. Lu, F. Ciucci, *J. Mater. Chem. A* **2016**, *4*, 17740.
[64] Z. Lu, C. Chen, Z. M. Baiyee, X. Chen, C. Niu, F. Ciucci, *Phys. Chem. Chem. Phys.* **2015**, *17*, 32547.
[65] J. P. Perdew, K. Burke, M. Ernzerhof, *Phys. Rev. Lett.* **1996**, *77*, 3865.
[66] P. E. Blöchl, *Phys. Rev. B* **1994**, *50*, 17953.
[67] D. J. Evans, B. L. Holian, *J. Chem. Phys.* **1985**, *83*, 4069.